

# Photon-number statistics with Silicon photomultipliers

Marco Ramilli,<sup>1</sup> Alessia Allevi,<sup>2</sup> Valery Chmill,<sup>1</sup> Maria Bondani,<sup>3,4,\*</sup>  
 Massimo Caccia,<sup>1</sup> and Alessandra Andreoni<sup>1,4</sup>

<sup>1</sup>*Dipartimento di Fisica e Matematica, Università degli Studi dell'Insubria  
 I-22100, Como, Italy*

<sup>2</sup>*CNISM, U.d.R. Milano Università, I-20133, Milano, Italy*

<sup>3</sup>*National Laboratory for Ultrafast and Ultraintense Optical Science - CNR-INFN, I-22100,  
 Como, Italy*

<sup>2</sup>*CNISM, U.d.R. Milano Università, I-20133, Milano, Italy*

<sup>4</sup>*CNISM, U.d.R. Como, I-22100, Como, Italy*

*\*Corresponding author: maria.bondani@uninsubria.it*

We present a description of the operation of a multi-pixel detector in the presence of non-negligible dark-count and cross-talk effects. We apply the model to devise self-consistent calibration strategies to be performed on the very light under investigation. © 2018 Optical Society of America

*OCIS codes:* 270.5290, 230.5160, 040.1240

## 1. Introduction

In the last decade many efforts have been devoted to the development and characterization of photon-number resolving detectors. The motivation stems from the variety of fields of applications: as an example, this kind of devices has already been used in particle physics experiments [1–6], PET systems [3, 7], biomedical research [8–12] and atmospheric pollution measurements [13, 14]. Moreover, there are other interesting fields of application in which photon-counting detectors could be exploited, such as LIDAR (light detection and ranging), laser scanning microscopy, and fluorescence correlation spectroscopy [15]. In addition, this class of detectors play a key role in quantum optics as it offers the possibility to characterize nonclassical multiphoton states. In this field they can be considered as a valid alternative to optical homodyne tomography [16] as they can be employed in direct detection schemes [17].

Several concepts and technologies have been proposed that lead to the development of detectors such as visible-light photon counters (VLPC) [18], superconductive transition edge sensors (TES) [19], time-multiplexed detectors [20–22], hybrid photodetectors (HPD) [23,24] and Silicon photomultipliers (SiPM) [25]. Irrespective of the concept and design features, these detectors may in general be classified in terms of photon detection efficiency, spectral response, time development of the signal, dead time, and notable photon number resolving capability. As of today, the ideal detector has yet to appear and the optimal choice is application specific.

This paper focuses on SiPMs, detectors featuring unique characteristics that are achieved by a rapidly evolving technology. Silicon photomultipliers consist of a high density (by now limited to  $\sim 2000$  cells/mm<sup>2</sup>) matrix of diodes with a common output. Each diode (or cell) is operated in a limited Geiger-Mueller (GM) regime, in order to achieve gains at the level of  $10^6$ . Quenching mechanisms are implemented to avoid establishing self-sustaining discharges. These detectors are sensitive to single photons triggering GM avalanches and can be endowed with a dynamic range well above 100 photons/burst. The photon detection efficiency (PDE) depends on the sensor design and specification, but it may well exceed 60%. Moreover, SiPM are genuine photon-number resolving detectors in that they measure light intensity simply by the number of fired diodes. Compactness, robustness, low cost, low operating voltage, and power consumption are also added values against traditional photodetectors. On the other hand, SiPMs are affected by significant dark count rates (DCR), associated to cells fired by thermally generated charge carriers. Moreover, the GM avalanche development is known to be associated to the generation of photons [26], which may in turn trigger secondary avalanches and result in relevant cross-talk. Whether DCR and cross-talk may be directly measured, it is clear that they are folded in the detector response to any signal and need to be modelled to properly assess the statistical properties of the light field being investigated. This paper reports the experimental validation of two models, on the way to a self-consistent characterization of the SiPM response.

## 2. Experimental set-up

The detector response to a weak light field is shown in Fig. 1(a), featuring the sensor output signal after a high-bandwidth amplifier with a gain of 50. The different bands in the image, obtained in persistency mode, correspond to samples with different numbers of triggered cells, i.e. different numbers of detected photons. The photon-number resolving properties are also clear in Fig. 1(b) that shows the corresponding spectrum as obtained by digitizing the amplified current pulse from the detector over a well defined time window, synchronized to the light pulse. These data and the results reported in the following were obtained with a SiPM produced by Hamamatsu Photonics [15]; more specifically, the main features of the

detector are reported in Table 1. We have decided to test a detector with  $10^2$  cells in order to keep DCR and cross-talk at a reasonable level and to maximize PDE. The signal was integrated by a charge digitizer V792 produced by Caen [27], with a 12-bit resolution over 400 pC range; the signal was typically integrated over a 200 ns long time window. The DCR and cross-talk can be directly obtained by measuring the frequency of the pulses from the sensor, with no illumination, above a well defined threshold. The result of a threshold scan of DCR is displayed in Fig. 2, clearly showing that the single cell avalanches stochastically triggered by thermally generated carriers can induce, by optical cross-talk, a cascade effect resulting in a multiple cell spurious event. Thus optical cross-talk can be measured using:

$$X_{talk} = \frac{\nu_2}{\nu_1} \quad (1)$$

where  $\nu_1$  is the the dark count rate measured by setting a threshold at a value lower than the peak amplitude of the signal corresponding to a single avalanche and  $\nu_2$  is the count rate obtained when the threshold is set beyond the single cell signals (see Figure 2). The experimental results reported below were obtained illuminating the sensor with a frequency-doubled Nd:YLF mode-locked laser amplified at 500 Hz (High Q Laser Production) that provides linearly polarized pulses of  $\sim 5.4$  ps duration at 523 nm wavelength. Two series of measurements were performed, the first one directly on the coherent laser output and the second one on the pseudo-thermal light obtained by passing the laser through a rotating ground-glass diffuser (D in Fig. 3) [28]. The light to be measured was delivered to the sensor by a multimode optical fiber (1 mm core diameter). The signal digitization was synchronized to the laser pulse.

### 3. Detector response modelling

The response of an ideal detector to a light field can be described in a simple way as a bernoullian process:

$$B_{m,n}(\eta) = \binom{n}{m} \eta^m (1 - \eta)^{n-m} , \quad (2)$$

being  $n$  the number of impinging photons over the integration time,  $m$  the number of detected photons and  $\eta < 1$  the photon-detection efficiency. Actually,  $\eta$  is a single parameter quantifying detector effects and losses (intentional or accidental) which can be tracked to the optical system. As far as SiPMs are concerned, detector effects are due to the quantum efficiency, the fill factor and the avalanche triggering probability, namely the probability for a charge carrier to develop a Geiger-Mueller quenched discharge [29, 30]. As a consequence, the distribution  $P_{m,el}$  of the number of detected photons, that is the GM avalanches actually corresponding to a detected photon has to be linked to the distribution  $P_{n,ph}$  of the number

of photons in the light under measurement by [31–33]:

$$P_{m,\text{el}} = \sum_{n=m}^{\infty} B_{m,n}(\eta) P_{n,\text{ph}} . \quad (3)$$

It can be demonstrated [24, 34] that for a combination of classical light states the statistics is preserved by the primary detection process. This simple description has to be further developed to link  $P_{m,\text{el}}$  to the probability density distribution of the GM avalanches of any origin. First we must take into account spurious hits and cross-talk effects, not negligible in the detectors being studied. The dark count rate results in a poissonian process which can be described as:

$$P_{m,\text{dc}} = \overline{m}_{\text{dc}}^m / m! \exp(-\overline{m}_{\text{dc}}) , \quad (4)$$

where  $\overline{m}_{\text{dc}}$  is the mean number of dark counts during the gate window (or integration time) and  $\sigma_{m,\text{dc}}^{(2)} = \sigma_{m,\text{dc}}^{(3)} = \overline{m}_{\text{dc}}$ .

As a consequence, the statistics of the recorded pulses may be described as:

$$P_{m,\text{el}+\text{dc}} = \sum_{i=0}^m P_{i,\text{dc}} P_{m-i,\text{el}} , \quad (5)$$

obviously shifting the mean value to  $\overline{m}_{\text{el}+\text{dc}} = \overline{m}_{\text{el}} + \overline{m}_{\text{dc}}$ , with an increased variance and third-order central moment  $\sigma_{m,\text{el}+\text{dc}}^{(2)} = \sigma_{m,\text{el}}^{(2)} + \sigma_{m,\text{dc}}^{(2)} = \sigma_{m,\text{el}}^{(2)} + \overline{m}_{\text{dc}}$  and  $\sigma_{m,\text{el}+\text{dc}}^{(3)} = \sigma_{m,\text{el}}^{(3)} + \sigma_{m,\text{dc}}^{(3)} = \sigma_{m,\text{el}}^{(3)} + \overline{m}_{\text{dc}}$ .

As a further step, cross-talk effects shall be taken into account. Cross-talk is a genuine cascade phenomenon that can be described at first order as [35]

$$C_{k,l}(\epsilon) = \binom{l}{k-l} \epsilon^{k-l} (1-\epsilon)^{2l-k} . \quad (6)$$

being  $\epsilon$  the (constant) probability that the GM avalanche of a cell triggers a second cell,  $l$  the number of dark counts and photo-triggered avalanches and  $k$  the actual light signal amplitude. Within this first-order approximation, the actual sensor response is described by

$$P_{k,\text{cross}} = \sum_{m=0}^k C_{k,m}(\epsilon) P_{m,\text{el}+\text{dc}} , \quad (7)$$

characterized by  $\overline{k}_{\text{cross}} = (1+\epsilon)\overline{m}_{\text{el}+\text{dc}}$ ,  $\sigma_{k,\text{cross}}^{(2)} = (1+\epsilon)^2\sigma_{m,\text{el}+\text{dc}}^{(2)} + \epsilon(1-\epsilon)\overline{m}_{m,\text{el}+\text{dc}}$  and  $\sigma_{k,\text{cross}}^{(3)} = (1+\epsilon)^3\sigma_{m,\text{el}+\text{dc}}^{(3)} + 3\epsilon(1-\epsilon^2)\sigma_{m,\text{el}+\text{dc}}^{(2)} + \epsilon(1-3\epsilon+2\epsilon^2)\overline{m}_{m,\text{el}+\text{dc}}$ . In the following we refer to this analytical model as *Model I*. We also consider a better refined model (*vide infra*, *Model II*) offering, in principle, an extended range of application, but paying the price of being limited to a numerical rather than analytical solution. Irrespective of the model, the

amplification and digitization processes that produces the output  $x$  can simply be described as a multiplicative parameter  $\gamma$ :

$$P_{x,\text{out}} = \gamma P_{\gamma k, \text{cross}} , \quad (8)$$

conveniently scaling the momenta as  $\bar{x}_{\text{out}} = \gamma \bar{k}_{\text{cross}}$ ,  $\sigma_{x,\text{out}}^{(2)} = \gamma^2 \sigma_{k,\text{cross}}^{(2)}$  and  $\sigma_{x,\text{out}}^{(3)} = \gamma^3 \sigma_{k,\text{cross}}^{(3)}$ .

### 3.A. Model I: an analytical evaluation of the second and third order momenta

This approach extends the method presented in [23] to detectors with a significant dark count rate and first order cross-talk effects. Experimentally, it is based on the detection of a light field performed by varying, in a controlled way, the optical losses, i.e.  $\eta$ , with detector parameters presumed to be constant throughout the  $\eta$  scan. The second-order momentum of the recorded pulse distribution  $P_{x,\text{out}}$  can be used to evaluate the Fano factor:

$$\begin{aligned} F_{x,\text{out}} &= \frac{\sigma_{x,\text{out}}^{(2)}}{\bar{x}_{\text{out}}} = \gamma \frac{\sigma_{k,\text{cross}}^{(2)}}{\bar{k}_{\text{cross}}} \\ &= \gamma(1 + \epsilon) \frac{\sigma_{m,\text{el+dc}}^{(2)}}{\bar{m}_{\text{el+dc}}} + \gamma \frac{\epsilon(1 - \epsilon)}{1 + \epsilon} \\ &= \frac{Q_{\text{el+dc}}}{\bar{m}_{\text{el+dc}}} \bar{x}_{\text{out}} + \gamma \frac{1 + 3\epsilon}{1 + \epsilon} , \end{aligned} \quad (9)$$

where  $Q_{\text{el+dc}} = \sigma_{m,\text{el+dc}}^{(2)}/\bar{m}_{\text{el+dc}} - 1$  is the Mandel factor of the primary charges. Note that, due to dark-counts, the coefficient of  $\bar{x}_{\text{out}}$  in Eq. (9) cannot be written as  $Q_{\text{ph}}/\bar{n}$  [23, 36], that is, the coefficient  $Q_{\text{el+dc}}/\bar{m}_{\text{el+dc}}$  does not only depend on the light field to be measured. Similarly we can calculate a sort of symmetry parameter

$$\begin{aligned} S_{x,\text{out}} &= \frac{\sigma_{x,\text{out}}^{(3)}}{\bar{x}_{\text{out}}} = \gamma^2 \frac{\sigma_{k,\text{cross}}^{(3)}}{\bar{k}_{\text{cross}}} \\ &= \gamma^2(1 + \epsilon)^2 \frac{\sigma_{m,\text{el+dc}}^{(3)}}{\bar{m}_{\text{el+dc}}} + 3\gamma^2 \epsilon(1 - \epsilon) \frac{\sigma_{m,\text{el+dc}}^{(2)}}{\bar{m}_{\text{el+dc}}} + \gamma^2 \frac{\epsilon(1 - 3\epsilon + 2\epsilon^2)}{1 + \epsilon} \\ &= \frac{Q_{s,\text{el+dc}} - 3Q_{\text{el+dc}}}{\bar{m}_{\text{el+dc}}^2} \bar{x}_{\text{out}}^2 + \gamma \frac{1 + 3\epsilon}{1 + \epsilon} \frac{Q_{\text{el+dc}}}{\bar{m}_{\text{el+dc}}} \bar{x}_{\text{out}} + \gamma^2 \frac{1 + 7\epsilon}{1 + \epsilon} , \end{aligned} \quad (10)$$

where  $Q_{s,\text{el+dc}} = \sigma_{m,\text{el+dc}}^{(3)}/\bar{m}_{\text{el+dc}} - 1$ . Note that in the presence of dark-counts both coefficients  $(Q_{s,\text{el+dc}} - 3Q_{\text{el+dc}})/\bar{m}_{\text{el+dc}}^2$  and  $Q_{\text{el+dc}}/\bar{m}_{\text{el+dc}}$  are no-more independent of the light under measurement [24]. We will see how this modifies the results in the following examples involving classical light states for which the statistics of detected photons is the same as that of photons.

A validation and a comparison of the proposed model was performed by sampling coherent and multi-thermal light fields, where the proposed model can be specified as follows.

### 3.A.1. Sampling a coherent light field

For a coherent field, the photon-number distribution is given by

$$P_{n,\text{ph}} = \frac{|\alpha|^{2n}}{n!} e^{-|\alpha|^2}, \quad (11)$$

for which  $\bar{n} = \sigma_n^{(2)} = \sigma_n^{(3)} = |\alpha|^2$ . Remembering that the distribution of dark-counts is also poissonian, according to Eq.s (9) and (10), we have:

$$\begin{aligned} \frac{Q_{\text{el+dc}}}{\bar{m}_{\text{el+dc}}} &= \frac{1}{\bar{m}_{\text{el+dc}}} \left[ \frac{\sigma_{m,\text{el+dc}}^{(2)}}{\bar{m}_{\text{el+dc}}} - 1 \right] = \frac{\sigma_{m,\text{el}}^{(2)} + \sigma_{m,\text{dc}}^{(2)} - (\bar{m}_{\text{el}} + \bar{m}_{\text{dc}})}{(\bar{m}_{\text{el}} + \bar{m}_{\text{dc}})^2} = 0 \\ \frac{Q_{s,\text{el+dc}} - 3Q_{\text{el+dc}}}{\bar{m}_{\text{el+dc}}^2} &= \frac{1}{\bar{m}_{\text{el+dc}}^2} \left[ \frac{\sigma_{m,\text{el+dc}}^{(3)}}{\bar{m}_{\text{el+dc}}} - 1 \right] = \frac{\sigma_{m,\text{el}}^{(3)} + \sigma_{m,\text{dc}}^{(3)} - (\bar{m}_{\text{el}} + \bar{m}_{\text{dc}})}{(\bar{m}_{\text{el}} + \bar{m}_{\text{dc}})^3} = 0. \end{aligned}$$

We thus obtain from Eq.s (9) and (10)

$$F_{x,\text{out}} = \gamma \frac{1 + 3\epsilon}{1 + \epsilon} \quad (12)$$

$$S_{x,\text{out}} = \gamma^2 \frac{1 + 7\epsilon}{1 + \epsilon} \quad (13)$$

at any mean value  $\bar{x}_{\text{out}}$ .

The results in Eq.s (12) and (13) show that, if we measure a coherent field at different values of  $\bar{x}_{\text{out}}$  by varying the overall detection efficiency  $\eta$  through an attenuator [23], we can obtain the values of  $\gamma$ , the detector gain, and  $\epsilon$ , the probability of cross-talk, by fitting the experimental values of  $F_{x,\text{out}}$  and  $S_{x,\text{out}}$ . The  $\gamma$ -value is obtained in units of  $x$  per detected photon. Of course, no information can be obtained from Eq.s (12) and (13) on the amount of dark-counts as far as the statistics is poissonian for both light and dark-counts. Note that, as the relation between  $\gamma$  and  $\epsilon$  is quadratic, we have in general two sets of possible values for each fit. The choice of one of the sets is made by comparing the value of  $\gamma$  with the interspacing between the peaks of the pulse-height spectrum.

### 3.A.2. Sampling a multi-mode thermal light field

The photon-number distribution of a field made of  $\mu$  independent thermal modes each containing  $N_{th}/\mu$  mean photons [31] is given by

$$P_{n,\text{ph}} = \frac{(n + \mu - 1)!}{n! (\mu - 1)! (N_{th}/\mu + 1)^\mu (\mu/N_{th} + 1)^n}, \quad (14)$$

for which  $\bar{n} = N_{th}$ ,  $\sigma_n^{(2)} = N_{th} (N_{th}/\mu + 1)$  and  $\sigma_n^{(3)} = N_{th} (N_{th}/\mu + 1) (2N_{th}/\mu + 1)$ . In this case we have

$$\frac{Q_{\text{el+dc}}}{\bar{m}_{\text{el+dc}}} = \frac{1}{\bar{m}_{\text{el+dc}}} \left[ \frac{\sigma_{m,\text{el+dc}}^{(2)}}{\bar{m}_{\text{el+dc}}} - 1 \right] = \frac{\sigma_{m,\text{el}}^{(2)} + \sigma_{m,\text{dc}}^{(2)} - (\bar{m}_{\text{el}} + \bar{m}_{\text{dc}})}{(\bar{m}_{\text{el}} + \bar{m}_{\text{dc}})^2}$$

$$\begin{aligned}
&= \frac{\overline{m}_{\text{el}}(\overline{m}_{\text{el}}/\mu + 1) + \overline{m}_{\text{dc}} - (\overline{m}_{\text{el}} + \overline{m}_{\text{dc}})}{(\overline{m}_{\text{el}} + \overline{m}_{\text{dc}})^2} = \frac{1}{\mu} \frac{\overline{m}_{\text{el}}^2}{(\overline{m}_{\text{el}} + \overline{m}_{\text{dc}})^2} \\
\frac{Q_{s,\text{el}+\text{dc}} - 3Q_{\text{el}+\text{dc}}}{\overline{m}_{\text{el}+\text{dc}}^2} &= \frac{1}{\overline{m}_{\text{el}+\text{dc}}^2} \left[ \frac{\sigma_{m,\text{el}+\text{dc}}^{(3)}}{\overline{m}_{\text{el}+\text{dc}}} - 1 - 3\frac{\sigma_{m,\text{el}+\text{dc}}^{(2)}}{\overline{m}_{\text{el}+\text{dc}}} + 3 \right] \\
&= \frac{\sigma_{m,\text{el}}^{(3)} + \sigma_{m,\text{dc}}^{(3)} - 3\sigma_{m,\text{el}}^{(2)} - 3\sigma_{m,\text{dc}}^{(2)} + 2(\overline{m}_{\text{el}} + \overline{m}_{\text{dc}})}{(\overline{m}_{\text{el}} + \overline{m}_{\text{dc}})^3} \\
&= \frac{\overline{m}_{\text{el}}(\overline{m}_{\text{el}}/\mu + 1)(2\overline{m}_{\text{el}}/\mu + 1) + \overline{m}_{\text{dc}} - 3\overline{m}_{\text{el}}(\overline{m}_{\text{el}}/\mu + 1) - 3\overline{m}_{\text{dc}} + 2(\overline{m}_{\text{el}} + \overline{m}_{\text{dc}})}{(\overline{m}_{\text{el}} + \overline{m}_{\text{dc}})^3} \\
&= \frac{2}{\mu^2} \frac{\overline{m}_{\text{el}}^3}{(\overline{m}_{\text{el}} + \overline{m}_{\text{dc}})^3}.
\end{aligned}$$

We now observe that the measured output mean value can be written as  $\overline{x}_{\text{out}} = \gamma(1+\epsilon)(\overline{m}_{\text{el}} + \overline{m}_{\text{dc}}) \equiv \overline{x}_{\text{ph}} + \overline{x}_{\text{dc}}$ , where only  $\overline{x}_{\text{ph}}$  undergoes attenuation during the experimental procedure while  $\overline{x}_{\text{dc}}$  remains constant. We thus rewrite Eq.s (9) and (10) as

$$F_{x,\text{out}} = \frac{1}{\mu} \left(1 - \frac{\overline{x}_{\text{dc}}}{\overline{x}_{\text{out}}}\right)^2 \overline{x}_{\text{out}} + \gamma \frac{1+3\epsilon}{1+\epsilon} \quad (15)$$

$$S_{x,\text{out}} = \frac{2}{\mu^2} \left(1 - \frac{\overline{x}_{\text{dc}}}{\overline{x}_{\text{out}}}\right)^3 \overline{x}_{\text{out}}^2 + \frac{3}{\mu} \gamma \frac{1+3\epsilon}{1+\epsilon} \left(1 - \frac{\overline{x}_{\text{dc}}}{\overline{x}_{\text{out}}}\right)^2 \overline{x}_{\text{out}} + \gamma^2 \frac{1+7\epsilon}{1+\epsilon}. \quad (16)$$

By measuring our multi-mode thermal field at different values of  $\overline{x}_{\text{out}}$ , and plotting  $F_{x,\text{out}}$  and  $S_{x,\text{out}}$  we can obtain an estimation of the parameters  $\mu$ ,  $\overline{x}_{\text{dc}}$ ,  $\epsilon$ ,  $\gamma$  from a self-consistent procedure and without need of an independent calibration. Again  $\gamma$  is in units of  $x$  per detected photon and the relation between  $\gamma$  and  $\epsilon$  is quadratic (see above).

### 3.B. Model II: a numerical evaluation based on the photon-number resolving properties of SiPM

The above mentioned self-consistent method is very powerful, but requires the acquisition of several histograms at varying  $\eta$ , which could not always be easy to perform, or possible at all, in many practical applications: from this point of view, the possibility to analyze each spectrum independently looks complementary to the self-consistent approach. We performed this analysis with a two-step procedure:

- we measured the areas of the spectrum peaks, thus obtaining an estimation of the number of counts per peak;
- we fitted the obtained data points with a theoretical function, which takes into account the statistics of light, detection and all deviations of the detectors from ideality, such as DCR and cross-talk effects.

To evaluate the area of each peak, we performed a multi-peak fit of the spectrum histogram, modelling each peak with a Gauss-Hermite function [37]:

$$\text{GH} = N e^{-w^2/2} \left[ 1 + {}^3h H_3(w) + {}^4h H_4(w) \right], \quad (17)$$

where

$$w = \frac{x - \bar{x}}{\sigma} \quad (18)$$

and  $N$  is a normalization factor,  $\bar{x}$  is the peak position and  $\sigma$  is the variance of the gaussian function;  $H_3(w)$  and  $H_4(w)$  are the third and the fourth normalized hermite polynomials and their contribution gives the asymmetry of the peak shape, whose entity is regulated by the pre-factors  ${}^3h$  and  ${}^4h$ , with values in the range  $[-1, 1]$ . The global fit function of the spectrum is a sum of as many Gauss-Hermite function as the number of resolved peaks.

The choice of the GH-function in Eq. (17) allows us to calculate the area  $A_n$  of the  $n$ -th peak in a very straightforward way, simply by the relation

$$A_n = N_n \sigma_n (\sqrt{2\pi} + {}^4h_n). \quad (19)$$

The error  $\sigma_{A_n}$  on the obtained value is calculated by propagating the errors on the fit parameters.

This analysis is also useful in order to calculate the system gain  $\gamma$ : in fact, from the fitted values of the peak positions  $\bar{x}_n$  we can calculate the peak-to-peak distance  $\Delta$  for all the resolved peaks:

$$\Delta_{n,n+1} = \bar{x}_{n+1} - \bar{x}_n. \quad (20)$$

The error  $\sigma_{\Delta_{n,n+1}}$  associated to this value is once again obtained by propagating the fit errors of the peak position values; furthermore, to estimate  $\gamma$  a weighted average on all the peak-to-peak values obtained from the analyzed histogram is performed.

As for the theoretical function, the effect of detection, DCR and amplification is modelled as described in previous sections (see Eq.s (2)-(5) and Eq. (8)).

The effect of cross-talk, is described by using a bernoullian process, in a way analogue to what has been done with function  $C_{k,m}(\epsilon)$  of Eq. (6). However, as cross-talk process is intrinsically a cascade phenomenon, its contribution has been calculated by adding higher order effects:

$$P_{k,cross} = \sum_{m=0}^k \sum_{n=0}^m \sum_{j=0}^n P_{k-m-n-j,el+dc} B_{m,k-m-n-j}(\epsilon) B_{n,m}(\epsilon) B_{j,n}(\epsilon); \quad (21)$$

where terms like  $B_{j,n}(\epsilon)$  stand for the bernoullian distribution

$$B_{j,n}(\epsilon) = \binom{n}{j} \epsilon^j (1 - \epsilon)^{n-j}. \quad (22)$$



Such a higher order expansion is not trivial to be achieved by the self-consistent approach of *Model I*, in which an explicit analytic expression of  $P_{x,\text{out}}$  is needed in order to calculate its momenta. Here, as all the elements of interest ( $\overline{m}_{\text{el}}$ ,  $\overline{m}_{\text{dc}}$ ,  $\epsilon$ , the number of modes  $\mu$ ) will be obtained as fit parameters, this is not necessary and therefore  $P_{x,\text{out}}$  can be just numerically calculated as the fitting function.

The major limitation of this approach is obvious: as all the information on the statistics of the system is obtained from the peak areas, this method can only be applied to peak-resolving histograms with a number of peaks greater than the number of free parameters of the fitting function, which, in the present analysis, can rise up to five.

## 4. Experimental results

### 4.A. Coherent light

First of all, we measured the coherent light emerging from the laser. We measured the values of the output,  $x$ , at 20000 subsequent laser shots for 15 series, each one with a different mean value  $\overline{x}_{\text{out}}$ , set by rotating a polarizer (P in Fig. 3) in front of the collection fiber. We then acquired a series of data in the absence of light and set the zero at the mean value of the main peak of the resulting histogram, in which the presence of dark counts and cross talk emerges as a much lower separated peak. Following *Model I* we evaluated the experimental values of  $F_{x,\text{out}}$  and  $S_{x,\text{out}}$  that are plotted in Fig. 4 as a function of  $\overline{x}_{\text{out}}$ . We then fitted the data to straight lines and obtained  $(81.1 \pm 0.2)$  ch, for  $F_{x,\text{out}}$ , and  $(6971 \pm 57)$  ch<sup>2</sup>, for  $S_{x,\text{out}}$ . These values were used to evaluate  $\gamma$  and  $\epsilon$  from Eqs. (12) and (13). We obtained  $\gamma = (75.4 \pm 1.3)$  ch and  $\epsilon = (0.039 \pm 0.009)$ . The  $x$ -values were then divided by  $\gamma$  and re-binned in unitary bins [23, 36] to obtain the  $P_{k,\text{cross}}$  distribution of the actual light signal amplitude measured in the presence of dark-counts and cross-talk. Note that due to the linearity of the detector the mean value of the output can be directly obtained as  $\overline{k}_{\text{cross}} = \overline{x}_{\text{out}}/\gamma$ , independent of the shape of the distribution.

In Fig. 5 we plot as bars six different  $P_{k,\text{cross}}$  distributions at different mean values. Superimposed to the experimental values we plot two theoretical curves, one is a poissonian (see Eq. (11)) having mean value  $\overline{k}_{\text{cross}}$  (white circles), while the other (full circles) is evaluated by including the cross-talk effect. We evaluate  $P_{k,\text{cross}}$  from Eq. (7) in the case in which  $P_{m,\text{el+dc}}$  is poissonian and get:

$$P_{k,\text{cross}} = e^{-\overline{m}_{\text{el+dc}}}(1 - \epsilon)^{-k} \epsilon^k {}_pF_q \left( 1, -k; \frac{1}{2} - \frac{k}{2}, 1 - \frac{m}{2}; -\frac{(1 - \epsilon)^2 \overline{m}_{\text{el+dc}}}{4\epsilon} \right) \frac{\sin(k\pi)}{k\pi}, \quad (23)$$

where  $\overline{m}_{\text{el+dc}} = \overline{k}_{\text{cross}}/(1 + \epsilon) = \overline{x}_{\text{out}}/(\gamma(1 + \epsilon))$ . The theoretical distributions (full circles in Fig. 5) are evaluated by using the measured values of  $\overline{x}_{\text{out}}$ ,  $\gamma$  and  $\epsilon$ .

Note that measuring a coherent light with this method enables the simultaneous characterization of the detector gain and of the contribution of cross-talk. The comparison between

the data and the theoretical functions can be estimated through the evaluation of the fidelity

$$f = \sum_{k=0}^m \sqrt{P_{k,\text{exp}} P_{k,\text{theo}}} . \quad (24)$$

On the other hand, using the method of analysis of *Model II*, we could study each one of the acquired histograms separately. As mentioned above, in the case of coherent light, we have a theoretical fitting function with a total of three free parameters: expectation value of light and DCR contribution  $\overline{m}_{\text{el}+\text{dc}}$ , the probability  $\epsilon$  for an avalanche to trigger a second one and a global normalization factor (up to three “iterations”): in this case we are limited to spectra with at least 4 resolved peaks.

In Fig. 6 we show the results of this analysis for the multi-peak fit and for the fit of the statistics of the avalanches using  $\chi^2$  as an indicator of the goodness of the fit result. The obtained  $\epsilon$  values are compatible with what we obtained with *Model I*. Also the gain values, evaluated as the peak-to-peak distance, show a good agreement with the  $\gamma$  values given by *Model I*:  $\gamma = (78.28 \pm 0.26)$  ch for spectrum in left panel and  $\gamma = (72.61 \pm 0.19)$  ch for spectrum in right panel.

#### 4.B. Multi-mode pseudo-thermal light

In order to obtain information on the contribution of dark-counts we have to measure a different light statistics, whose shape is modified by the convolution with the poissonian distribution for dark-counts. We thus produced a pseudo-thermal light field by selecting with a small aperture ( $\sim 150 \mu\text{m}$  diameter) a region much smaller than the coherence area of the speckle patterns produced by the rotating diffuser. We follow the same procedure described for coherent light by measuring the values of the output,  $x$ , at 50000 subsequent laser shots and at 10 different mean values, obtained by means of a variable neutral-density filter (ND in Fig. 3). In Fig. 7 we plot the experimental values of  $F_{x,\text{out}}$  and  $S_{x,\text{out}}$  as a function of  $\overline{x}_{\text{out}}$ . Along with the experimental data we plot the fitting curves evaluated according to Eqs. (15) and (16). To describe the fitting procedure in detail we rewrite Eqs. (15) and (16) as the

$$F_{x,\text{out}} = \left(1 - \frac{\overline{x}_{\text{dc}}}{\overline{x}_{\text{out}}}\right)^2 \overline{x}_{\text{out}} + B \quad (25)$$

$$S_{x,\text{out}} = A \left(1 - \frac{\overline{x}_{\text{dc}}}{\overline{x}_{\text{out}}}\right)^3 \overline{x}_{\text{out}}^2 + 3B \left(1 - \frac{\overline{x}_{\text{dc}}}{\overline{x}_{\text{out}}}\right)^2 \overline{x}_{\text{out}} + C , \quad (26)$$

where we have set  $\mu = 1$ . First of all we fitted the data to  $F_{x,\text{out}}$  and obtained the values of  $\overline{x}_{\text{dc}} = (5.82028 \pm 1.34015)$  and  $B = (87.805 \pm 2.09009)$  ch. Then we fitted the data for  $S_{x,\text{out}}$  by substituting the obtained values of  $\overline{x}_{\text{dc}}$  ch and  $B$  to obtain  $A = (2.34754 \pm 0.091576)$  and  $C = (8531.48 \pm 419.571)$  ch<sup>2</sup>. These values are then used to evaluate  $\gamma$  and  $\epsilon$  from Eqs. (15) and (16). We obtained  $\gamma = (74.2785 \pm 18.6017)$  ch and  $\epsilon = (0.100174 \pm 0.166894)$ .

The  $x$ -values were then divided by  $\gamma$  and re-binned in unitary bins [23] to obtain the  $P_{k,\text{cross}}$  distribution of the actual light signal amplitude measured in the presence of dark-counts and cross-talk. In Fig. 8 we plot, as bars, six different  $P_{k,\text{cross}}$  distributions at different mean values. Superimposed to the experimental values we plot two theoretical distributions: the first one (open circles) is evaluated by including the contribution of dark-count that modifies the statistics of a single-mode thermal distribution (see Eq. (14)) into  $P_{m,\text{el+dc}}$  according to Eq. (27), which, in the present case, yields:

$$\begin{aligned} P_{m,\text{el+dc}} &= \sum_{k=0}^m P_{k,\text{dc}} P_{m-k,\text{el}} \\ &= \frac{e^{-\overline{m}_{\text{dc}}}}{(\mu-1)!} \left(1 + \frac{\mu}{\overline{m}_{\text{el}}}\right)^{-m} \left(1 + \frac{\overline{m}_{\text{el}}}{\mu}\right)^{-\mu} U\left[-m, 1-m-\mu, \overline{m}_{\text{dc}} \left(1 + \frac{\mu}{\overline{m}_{\text{el}}}\right)\right] \end{aligned} \quad (27)$$

where  $U(a, b, z)$  is the confluent hypergeometric function. The parameters are evaluated as  $\overline{m}_{\text{dc}} = \overline{x}_{\text{dc}}/(\gamma(1+\epsilon))$  and  $\overline{m}_{\text{el}} = (\overline{x}_{\text{out}} - \overline{x}_{\text{dc}})/(\gamma(1+\epsilon))$ . The second distribution (full circles) is evaluated from Eq. (7) to take into account the cross-talk. Unfortunately, the calculation does not yield an easy analytical result, and hence we evaluate it numerically. The values of the fidelity for the data in Fig. 8 improve when we take into account both dark-counts and cross-talk.

Turning now to the other approach, we note how the number of fit parameters in this case is enhanced: we now have the expectation value  $\overline{m}_{\text{el}}$  of avalanches generated by detection, the expectation value  $\overline{m}_{\text{dc}}$  of DCR contribution, the number of modes  $\mu$ , the probability  $\epsilon$  of triggering a cross-talk event (up to three iterations) and again a global normalization factor, for a total of 5 fit parameters: obviously, this puts a severe limit on the applicability of this method, needing at least 6 resolved peaks.

As it can be noted from the fit results in Fig. 9, once again the results obtained by using *Model II* are compatible within errors with what we found by applying *Model I*. However, whether the global fits present a very low  $\chi^2$  value for degree of freedom, the obtained fit parameters present high uncertainties, probably indicating the presence of very high off-diagonal elements in the minimization matrix and suggesting a strong correlation between the various parameters. This problem can be avoided by fixing some of the fit parameters (such as DCR or cross-talk), by retrieving their value from an accurate direct measurement as that explained in Section 2.

## 5. Discussion

We can compare the results of the two analysis methods on the same data-sets taken at different intensities. In Fig. 10 (a) we plot as full circles the values of  $\epsilon$  obtained by applying *Model II* to coherent light along with their weighted average (full line). As a comparison, the value of  $\epsilon$  obtained by applying *Model I* is plotted as dashed line. In Fig. 10 (b) we plot

as full circles the values of mean photon numbers evaluated for the same data as in panel (a) by applying *Model II*. White circles represent the values of mean photon numbers obtained by applying *Model I*. As we can see, the values are compatible within errors.

The same comparison for the measurements on thermal light is shown in Fig. 11. Here we can see that the agreement is better for the mean values of detected photons (panel (a)) and for the DCR (panel (b)), while the estimated values of  $\epsilon$  from the two *Models* definitely disagree. This can be due to the different approximations adopted by the two *Models* (first order *vs* third order) that become relevant when measuring thermal light instead of coherent light.

In Table 2 we summarize the results of the two *Models*. We demonstrated that both the *Models* work in a self-consistent way, even if they have two definitely different approaches. *Model I* does not need peak resolving capability, but requires the acquisition of several histograms at varying  $\eta$ . Once determined the parameters  $\epsilon$  and DCR, all the data-sets in a series can be analyzed, independent of the number of distinguishable peaks in the pulse-height spectrum. *Model II* works analyzing each histogram independently, but, as GM-avalanches distribution is obtained with a fit of the data, it requires at least a number of resolved peaks greater than the number of free parameters. The fact that the two *Models* give very similar results for mean photon numbers is particularly important as in most applications this is the only important parameter. Merging the two *Models* we can devise an optimal strategy based on a self-consistent calibration performed by measuring a known light and analyzing the data with *Model I*: once known  $\epsilon$  and DCR, the determination of the mean photon number is independent of the specific statistics of light. Hence the information on the mean photon number can be obtained from each single measurement, even when the fitting procedure of *Model II* cannot be applied.

## 6. Conclusions

We have developed a model to describe the operation of a multi-pixel detector for which dark-count and cross-talk effects are non negligible and we have implemented two different procedures for recovering the values of dark-counts and cross-talk, both implemented on measurements performed on the same light under characterization. We demonstrated that *Model I* is self-consistent and does not need peak resolving capability; on the other hand, it requires the acquisition of several histograms at varying  $\eta$ . *Model II* works by analyzing each histogram independently, but seems to be a less robust method in order to perform direct measurements of the detector parameters and it is better performing if supported with direct measurement of some relevant parameters. The results obtained by both methods show that the light statistics can be reliably reconstructed in the case of coherent and thermal light.

## Acknowledgments

Part of the equipment used has been funded by the European Commission within the RAPSODI Project - COOP 32993.

## References

1. N. Kanaya, "HPD for linear colliders for the JLC calorimeter group," Nucl. Instrum. Methods Phys. Res. A **442**, 295-299 (2000).
2. P. Buzhan et al., "Silicon photomultiplier and its possible applications," Nucl. Instrum. Methods Phys. Res. A **504**, 48-52 (2003).
3. B. Dolgoshein et al., "Status report on silicon photomultiplier development and its applications," Nucl. Instrum. Methods Phys. Res. A **563**, 368-376 (2006).
4. J. Haba, "Status and perspectives of Pixelated Photon Detector (PPD)," Nucl. Instrum. Methods Phys. Res. A **595**, 154-160 (2008).
5. S. Korpar et al., "Silicon photomultiplier as a detector of Cherenkov photons," Nucl. Instrum. Methods Phys. Res. A **595**, 161-164 (2008).
6. S. Takeshita et al., "Development of positron detector for mSR based on multi-pixel photoncounter," Nucl. Instrum. Methods Phys. Res. A **600**, 139-142 (2009).
7. S. Moehrs, A. Del Guerra, D.J. Herbert, and M.A. Mandelkern, "A detector head design for small-animal PET with silicon photomultipliers (SiPM)," Phys. Med. Biol. **51**, 1113-1127 (2006).
8. E. Grigoriev et al., "Silicon photomultipliers and their bio-medical applications," Nucl. Instrum. Methods Phys. Res. A **571**, 130-133 (2007).
9. S. Gomi et al., "Development and study of the multi pixel photon counter," Nucl. Instrum. Methods Phys. Res. A **581**, 427-432 (2007).
10. C. Cappellini et al., "The RAPSODI project: SiPM development for applied research in radiation protection," Nuclear Science Symposium Conference Record, 2008. NSS '08. IEEE, 1069-1072 (2009).
11. D. Fukuda et al., "Photon number resolving detection with high speed and high quantum efficiency," Metrologia **46**, S288-S292 (2009).
12. F. Risigo, A. Bulgheroni, M. Caccia, C. Cappellini, V. Chmill, N. Feduyushkina, A. Golubev, M. Jastrzab, A. Kantsyrev, N. Markov, A. Martemianov, C. Pychlau, J. Würfel, "SiPM technology applied to radiation sensor development," Nucl. Instrum. Methods Phys. Res. A, **607**, 7577 (2009).
13. D. Kedar and S. Arnon, "Subsea ultraviolet solar-blind broadband free-space optics communication," Opt. Eng. **48**, 046001(1-7) (2009).

14. S. Arnon and D. Kedar, "Non-line-of-sight underwater optical wireless communication network," *J. Opt. Soc. Am. A* **26**, 530-539 (2009).
15. <http://www.hamamatsu.com>
16. For a review, see A. I. Lvovsky and M. G. Raymer, "Continuous-variable optical quantum state tomography," *Rev. Mod. Phys.* **81**, 299-332 (2009).
17. M. Bondani, A. Allevi, and A. Andreoni, "Wigner function of pulsed fields by direct detection," *Opt. Lett.* **34**, 1444-1446 (2009).
18. J. Kim, S. Takeuchi, Y. Yamamoto and H. H. Hogue, "Multiphoton detection using visible light photon counter," *Appl. Phys. Lett.* **74**, 902-904 (1999).
19. A. E. Lita, A. J. Miller, and S. W. Nam, "Counting near-infrared single photons with 95% efficiency," *Opt. Expr.* **16**, 3032-3040 (2008).
20. D. Achilles et al., "Photon-number-resolving detection using time-multiplexing," *J. Mod. Opt.* **51**, 1499-1515 (2004).
21. K. Laiho, M. Avenhaus, K. N. Cassemiro and Ch. Silberhorn, "Direct probing of the Wigner function by time-multiplexed detection of photon statistics," *New J. Phys.* **11**, 043012(1-21) (2009).
22. M. Mičuda, O. Haderka and M. Ježek, "High-efficiency photon-number-resolving multi-channel detector," *Phys. Rev. A* **78**, 025804(1-4) (2008).
23. M. Bondani, A. Allevi, A. Agliati, and A. Andreoni, "Self-consistent characterization of light statistics," *J. Mod. Opt.* **56**, 226-231 (2009).
24. M. Bondani, A. Allevi, and A. Andreoni, "Light statistics by non-calibrated linear photodetectors," *Adv. Sci. Lett.* **2**, 463-468 (2009).
25. A. V. Akindinov, A. N. Martemianov, P. A. Polozov, V. M. Golovin, and E. A. Grigoriev, "New results on MRS APDs," *Nucl. Instr. and Meth. in Phys. Res. A* **387**, 231-234 (1997).
26. F. Zappa, S. Cova, M. Ghioni, A. Lacaita, C. Samori, "Avalanche photodiodes and quenching circuits for single-photon detection," *Appl. Opt.* **35**, 1956-1976 (1996).
27. <http://www.caen.it>
28. F. T. Arecchi, "Measurement of the Statistical Distribution of Gaussian and Laser Sources," *Phys. Rev. Lett.* **15**, 912-916 (1965).
29. K. G. McKay, "Avalanche Breakdown in Silicon," *Phys. Rev.* **94**, 877-884 (1954).
30. W. G. Oldham, R. R. Samuelson, P. Antognetti, "Triggering phenomena in avalanche diodes," *IEEE Trans. Electron. Dev.* **ED-19**, 1056-1060 (1972).
31. L. Mandel and E. Wolf, *Optical Coherence and Quantum Optics* (Cambridge University Press, New York, NY, 1995).
32. A. Agliati, M. Bondani, A. Andreoni, G. De Cillis and M. G. A. Paris, "Quantum and classical correlations of intense beams of light via joint photodetection," *J. Opt. B:*

- Quantum Semiclassical Opt. **7**, S652-S663 (2005).
33. G. Zambra, M. Bondani, A. S. Spinelli, and A. Andreoni, “Counting photoelectrons in the response of a photomultiplier tube to single picosecond light pulses,” *Rev. Sci. Instrum.* **75**, 2762-2765 (2004).
  34. E. Casini and A. Martinelli, “A family of distributions stable with respect to random sums”. Manuscript in preparation.
  35. I. Afek, A. Natan, O. Ambar, and Y. Silberberg, “Quantum state measurements using multipixel photon detectors,” *Phys. Rev. A* **79**, 043830(1-6) (2009).
  36. A. Andreoni and M. Bondani, “Photon statistics in the macroscopic realm measured without photon counters,” *Phys. Rev. A* **80**, 013819(1-5) (2009).
  37. R. P. Van Der Marel and M. Franx, “A new method for the identification of non-gaussian line profiles in elliptical galaxies,” *Astrophys. J.* **407**, 525-539 (1993).

Fig. 1. Left panel: Output of a SiPM Hamamatsu MPPC S10362-11-100C detecting a weak light field as displayed by a 100 MHz oscilloscope. Right panel: histogram of the corresponding spectrum.

Fig. 2. Threshold scan of the SiPM performed at room temperature with no impinging light.

Fig. 3. (Color online) Experimental setup. Nd:YLF: laser source, P: polaroid, ND: variable neutral density filter, SiPM: detector. The components in the dashed boxes are inserted to produce the pseudo-thermal field.

Fig. 4. (Color online) Plot of  $F_{x,\text{out}}$  and  $S_{x,\text{out}}$  as a function of  $\bar{x}_{\text{out}}$  for coherent light.

Fig. 5. (Color online) Experimental  $P_{k,\text{cross}}$  distributions at different mean values (bars) and theoretical curves evaluated according to *Model I*: poissonian (white circles), poissonian modified by cross-talk effect (full circles). The corresponding fidelity values of the reconstruction are also shown.

Fig. 6. (Color online) Experimental results for *Model II* applied on two of the histograms acquired with coherent light. Upper row: result of the multi-peak fit procedure; lower row: fitted theoretical distributions. The corresponding fidelity values of the reconstruction are also shown.

Fig. 7. (Color online) Plot of  $F_{x,\text{out}}$  and  $S_{x,\text{out}}$  as a function of  $\bar{x}_{\text{out}}$  for pseudo-thermal light.

Fig. 8. (Color online) Experimental  $P_{k,\text{cross}}$  distributions at different mean values (bars) and theoretical distributions evaluated according to *Model I*: thermal modified by dark count distribution (white circles), thermal modified by dark counts and cross-talk effect (full circles). The corresponding fidelity values of the reconstruction are also shown.

Fig. 9. (Color online) Experimental results for *Model II* applied on two of the histograms acquired with thermal light. Upper row: result of the multi-peak fit procedure; lower row: fitted theoretical function. The corresponding fidelity values of the reconstruction are also shown.

Fig. 10. (Color online) Left panel: values of  $\epsilon$  obtained by applying *Model II* to coherent light (full circles) and their weighted average (full line). Dashed line: value of  $\epsilon$  obtained by *Model I*. Right panel: values of mean photon numbers evaluated by applying *Model II* (full circles) and by applying *Model I* (white circles).

Fig. 11. (Color online) Left panel: values of  $\epsilon$  obtained by applying *Model II* to thermal light (full circles) and their weighted average (full line). Dashed line: value of  $\epsilon$  obtained by *Model I*. Central panel: values of DCR evaluated for the same data as in the left panel by applying *Model II* (full circles) and their weighted average (full line). Dashed line: value of DCR obtained by *Model I*. Right panel: values of mean photon numbers evaluated by applying *Model II* (full circles) and by applying *Model I* (white circles).



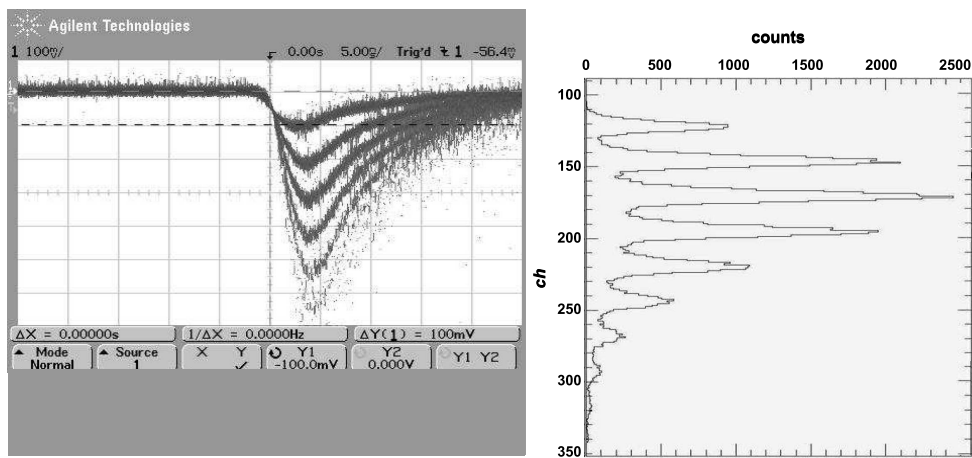


Fig. 1. Left panel: Output of a SiPM Hamamatsu MPPC S10362-11-100C detecting a weak light field as displayed by a 100 MHz oscilloscope. Right panel: histogram of the corresponding spectrum.

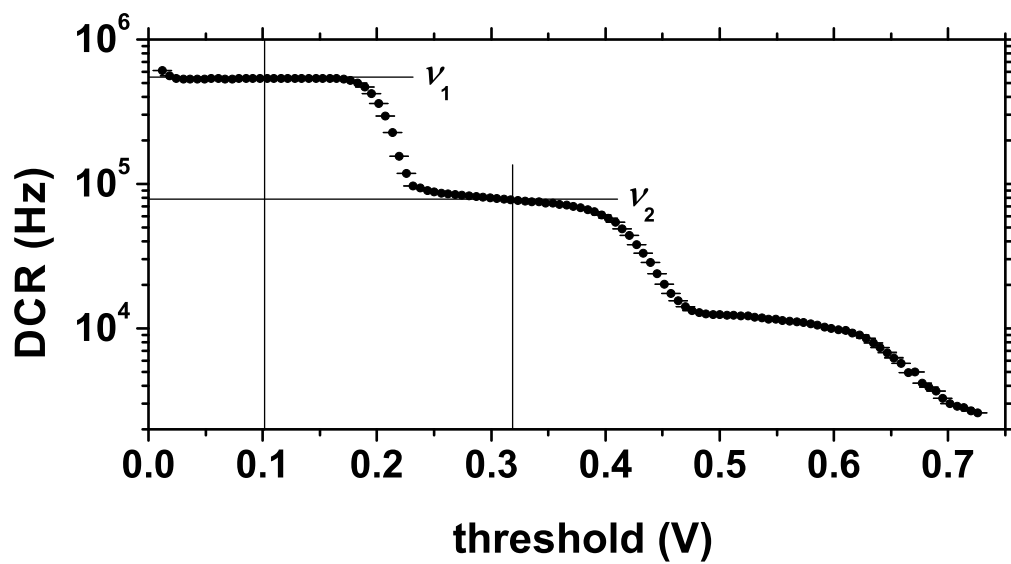


Fig. 2. DCR threshold scan of the SiPM performed at room temperature with no impinging light.

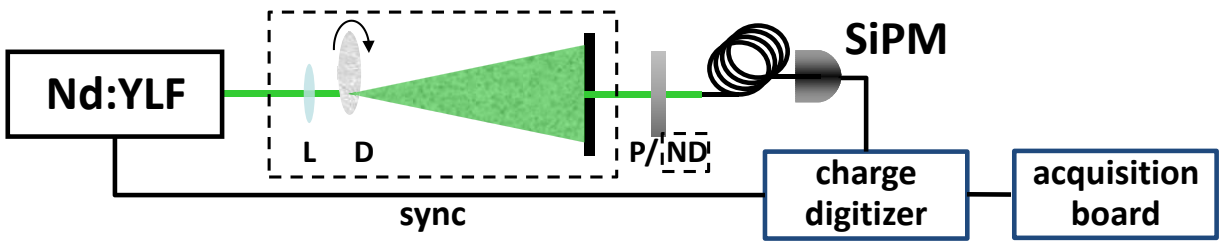


Fig. 3. (Color online) Experimental setup. Nd:YLF: laser source, P: polaroid, ND: variable neutral density filter, SiPM: detector. The components in the dashed boxes are inserted to produce the pseudo-thermal field.

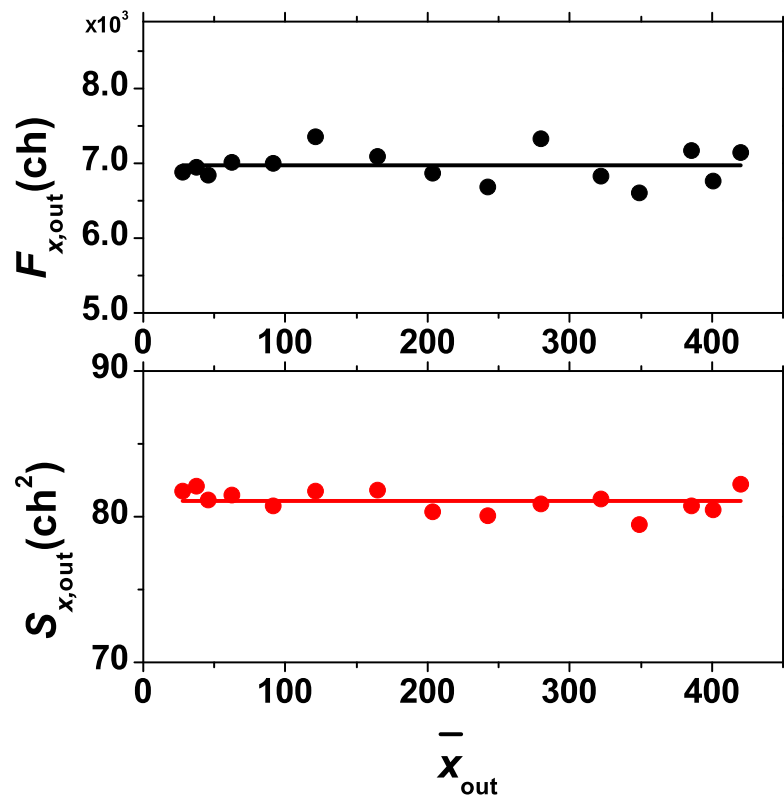


Fig. 4. (Color online) Plot of  $F_{x,out}$  and  $S_{x,out}$  as a function of  $\bar{x}_{out}$  for coherent light.

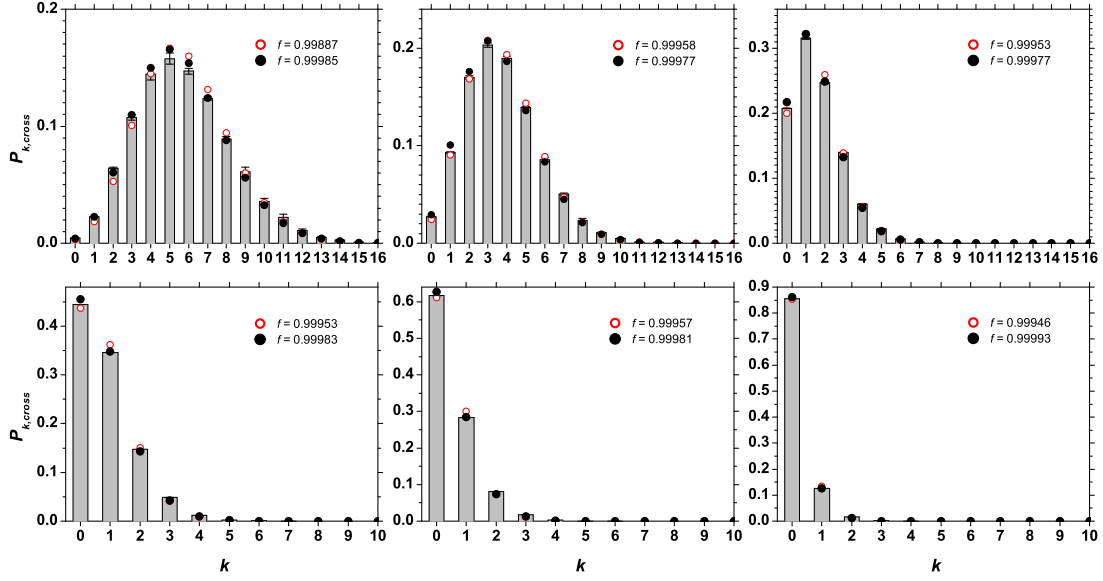


Fig. 5. (Color online) Experimental  $P_{k,cross}$  distributions at different mean values (bars) and theoretical curves evaluated according to *Model I*: poissonian (white circles), poissonian modified by cross-talk effect (full circles). The corresponding fidelity values of the reconstruction are also shown.

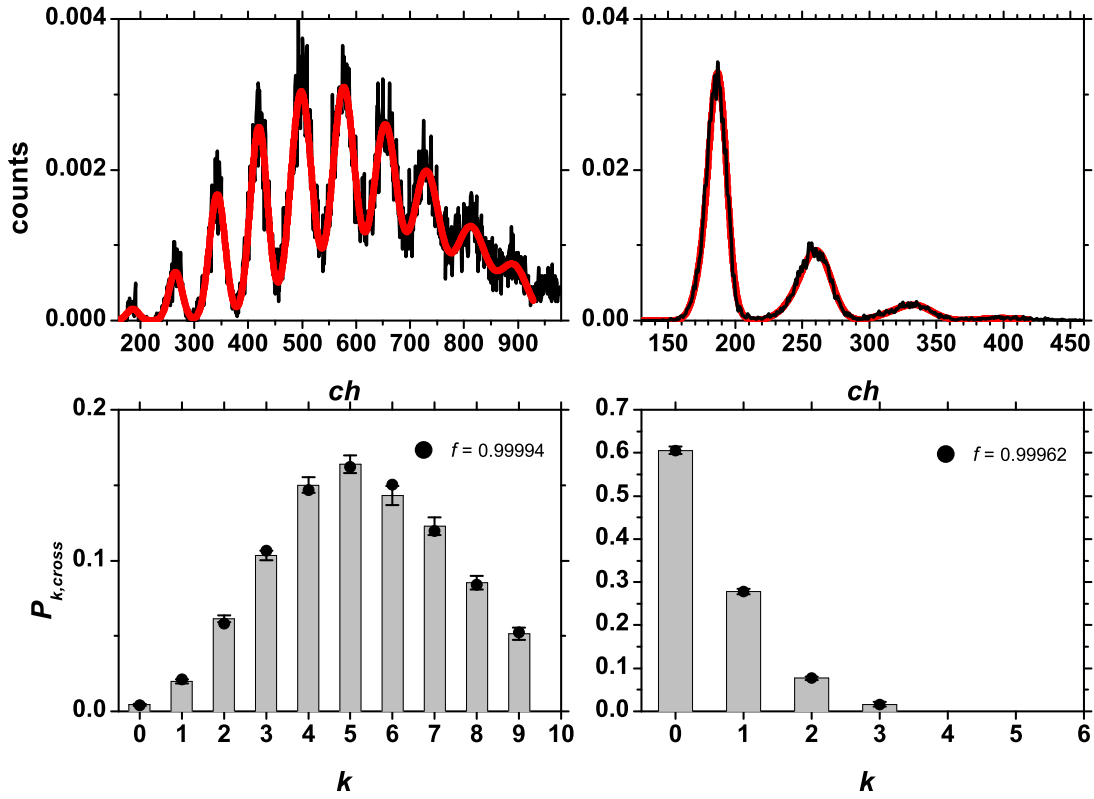


Fig. 6. (Color online) Experimental results for *Model II* applied on two of the histograms acquired with coherent light. Upper row: result of the multi-peak fit procedure; lower row: fitted theoretical distributions. The corresponding fidelity values of the reconstruction are also shown.

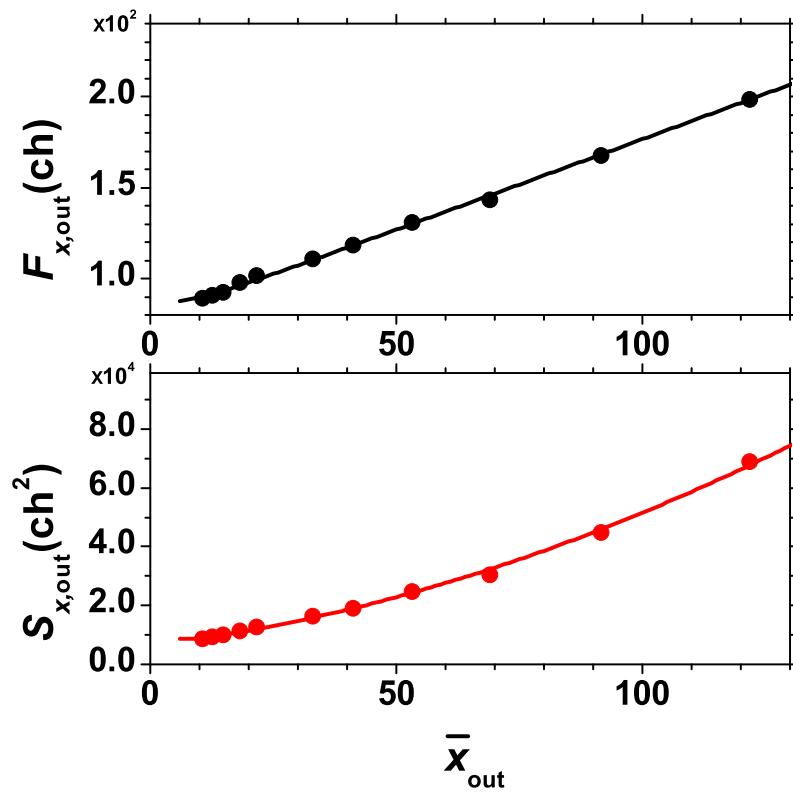


Fig. 7. (Color online) Plot of  $F_{x,out}$  and  $S_{x,out}$  as a function of  $\bar{x}_{out}$  for pseudo-thermal light.

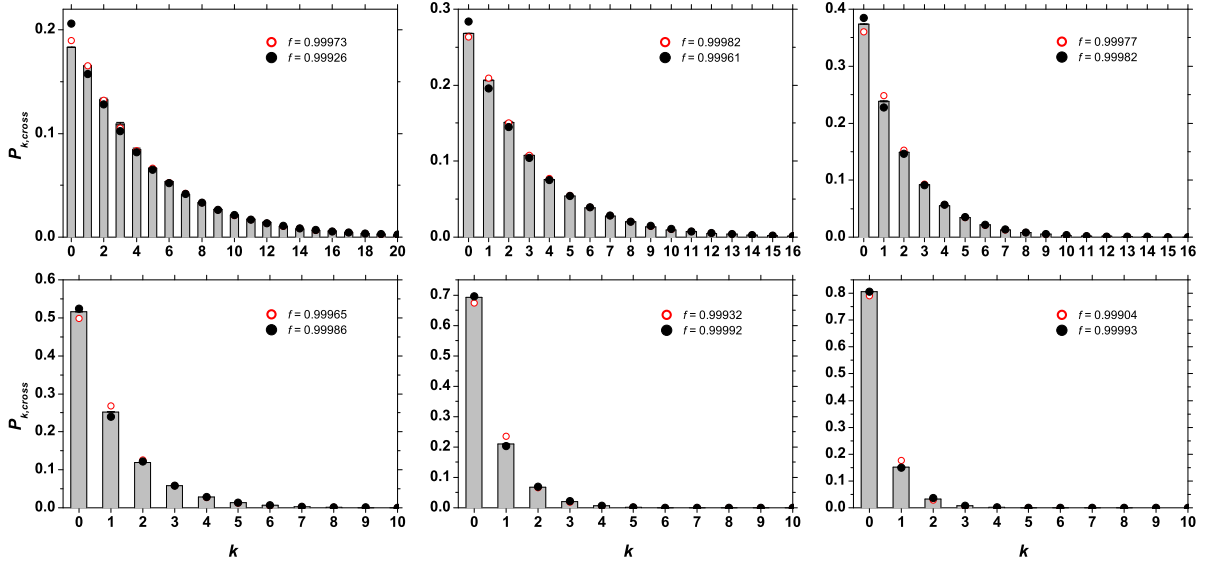


Fig. 8. (Color online) Experimental  $P_{k,cross}$  distributions at different mean values (bars) and theoretical distributions evaluated according to *Model I*: thermal modified by dark count distribution (white circles), thermal modified by dark counts and cross-talk effect (full circles). The corresponding fidelity values of the reconstruction are also shown.



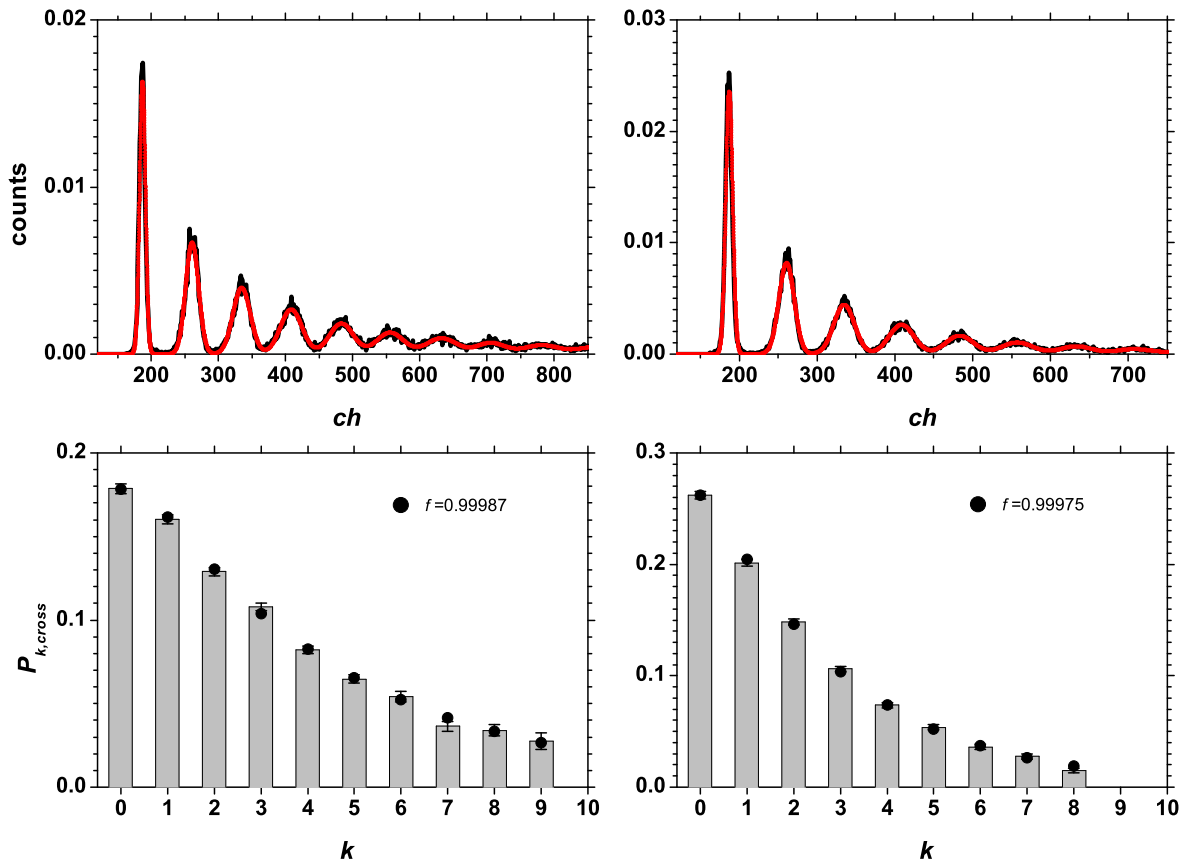


Fig. 9. (Color online) Experimental results for *Model II* applied on two of the histograms acquired with thermal light. Upper row: result of the multi-peak fit procedure; lower row: fitted theoretical function. The corresponding fidelity values of the reconstruction are also shown.

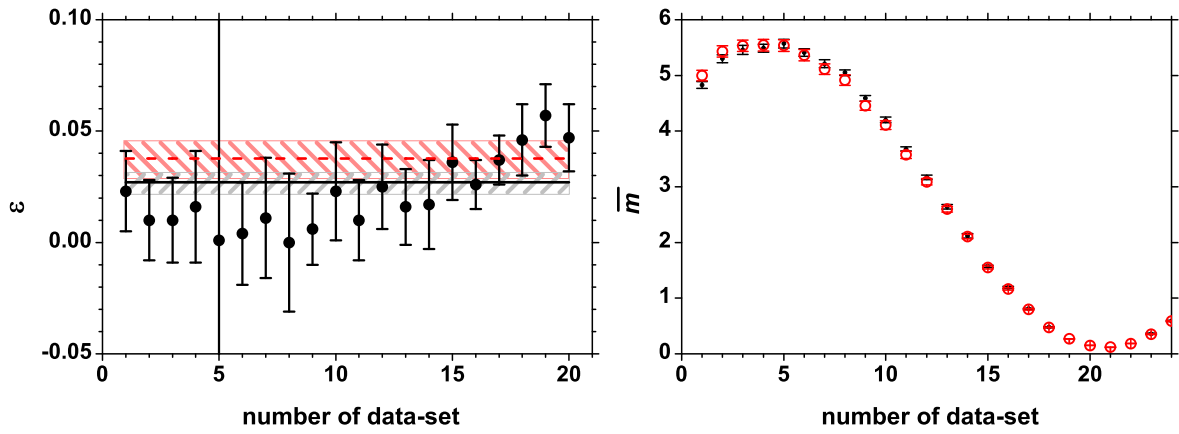


Fig. 10. (Color online) Left panel: values of  $\epsilon$  obtained by applying *Model II* to coherent light (full circles) and their weighted average (full line). Dashed line: value of  $\epsilon$  obtained by *Model I*. Right panel: values of mean photon numbers evaluated by applying *Model II* (full circles) and by applying *Model I* (white circles).

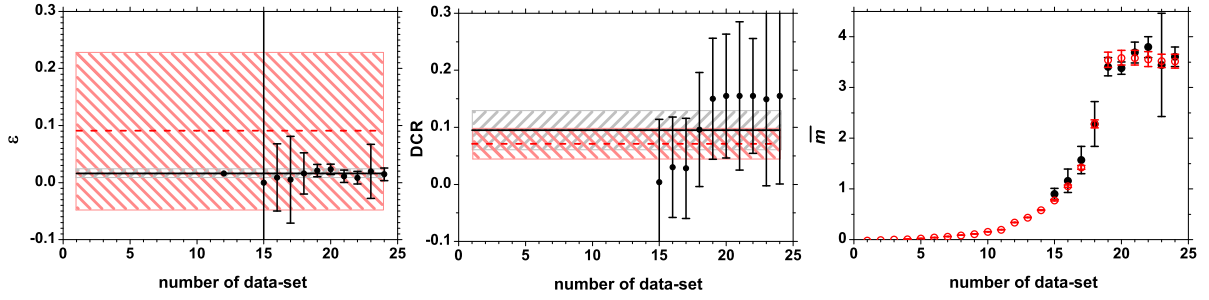


Fig. 11. (Color online) Left panel: values of  $\epsilon$  obtained by applying *Model II* to thermal light (full circles) and their weighted average (full line). Dashed line: value of  $\epsilon$  obtained by *Model I*. Central panel: values of DCR evaluated for the same data as in the left panel by applying *Model II* (full circles) and their weighted average (full line). Dashed line: value of DCR obtained by *Model I*. Right panel: values of mean photon numbers evaluated by applying *Model II* (full circles) and by applying *Model I* (white circles).

Hamamatsu MPPC S10362-11-100C	
Number of Diodes:	100
Area:	1 mm $\times$ 1 mm
Diode dimension:	100 $\mu\text{m}$ $\times$ 100 $\mu\text{m}$
Breakdown Voltage:	69.23 V
dark-count Rate:	540 kHz at 70 V
Optical Crosstalk:	25 % at 70 V
Gain:	$3.3 \cdot 10^6$ at 70 V
PDE (green):	15 % at 70 V

Table 1. Main characteristics of the SiPM (Hamamatsu, model MPPC S10362-11-100C). The data refer to room temperature.

	Poissonian		Pseudo-thermal	
	<i>Model I</i>	<i>Model II</i>	<i>Model I</i>	<i>Model II</i>
DCR	-	-	$0.071 \pm 0.027$	$0.094 \pm 0.035$
$\epsilon$	$0.038 \pm 0.008$	$0.027 \pm 0.005$	$0.091 \pm 0.138$	$0.035 \pm 0.004$

Table 2. Comparison between the global DCR and cross-talk values obtained with *Model I* and weighted average of the values obtained with *Model II*.